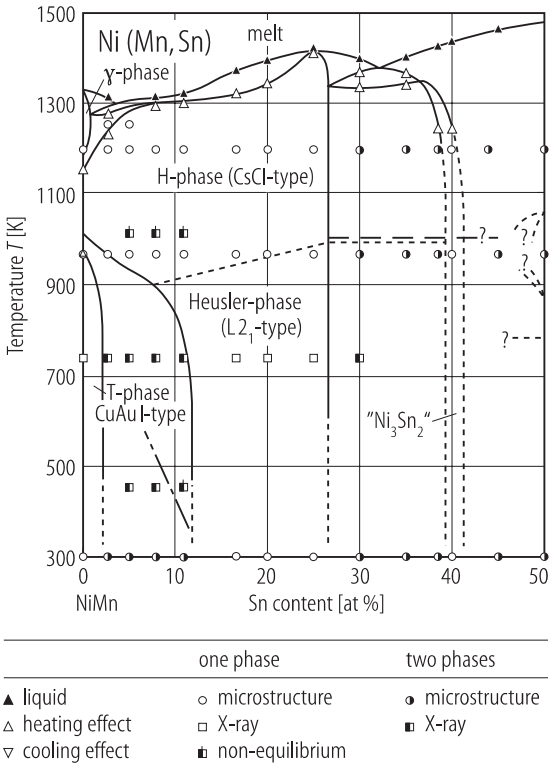

Fig. 8. Vertical section of the phase diagram of Ni(Mn,Sn) system for a constant 50 at% Nickel concentration [83W1].

Ni–Fe–Al

The phase diagram was investigated with the aim of obtaining a high creep resistance in intermetallic phases.

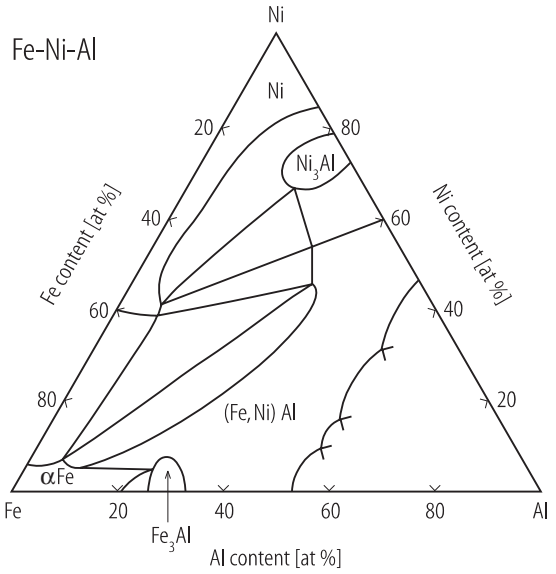

Fig. 9. Isothermal section at 400 °C of the Fe–Ni–Al phase diagram [87J1].

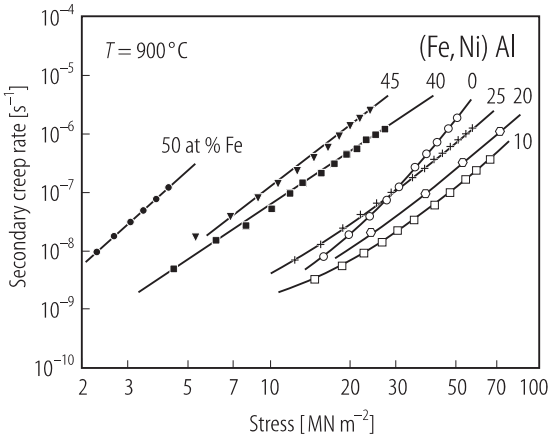

Fig. 10. Stress dependence of the secondary creep rate of various stoichiometric (Fe,Ni)Al phases at 900 °C [87J1].

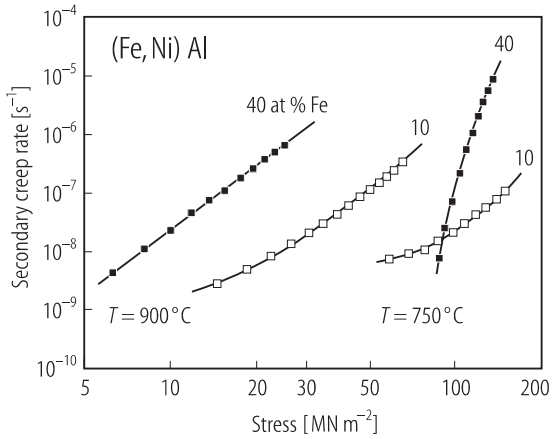

Fig. 11. Stress dependence of the secondary creep rate of $(Fe_{0.8}Ni_{0.2})Al$ and $(Ni_{0.8}Fe)Al$ at 750 °C and 900 °C [87J1].

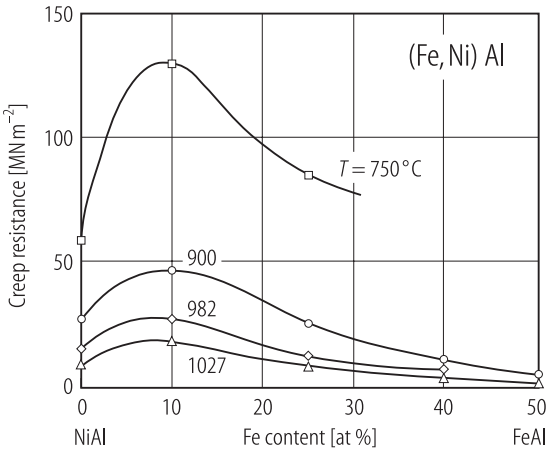

Fig. 12. Creep resistance (at 10^{-7} s^{-1}) as a function of iron content for stoichiometric (Fe,Ni)Al at 750 °C, 900 °C, 982 °C, and 1027 °C [87J1].

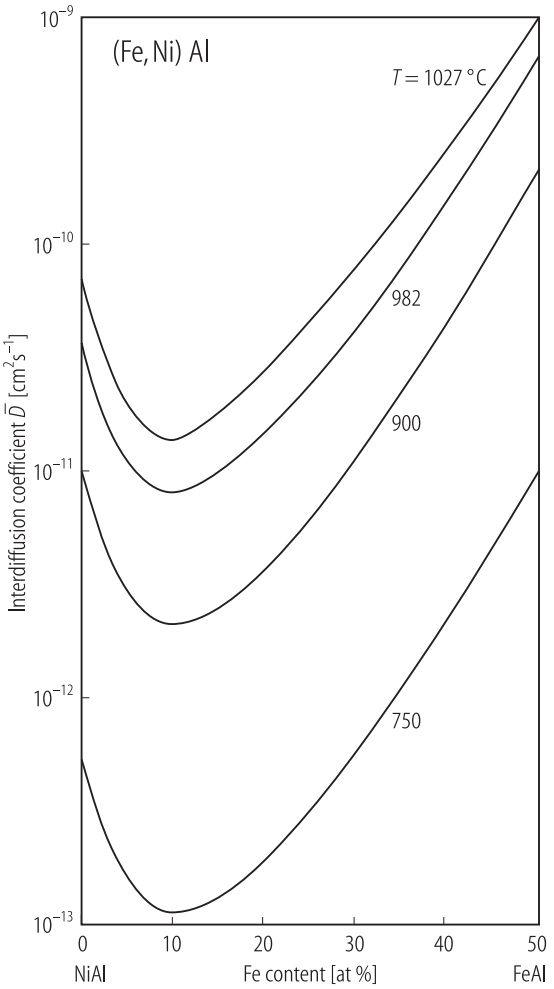

Fig. 13. Estimated interdiffusion coefficient $\bar{D}$ of stoichiometric (Fe,Ni)Al as a function of iron content for various temperatures [87J1].

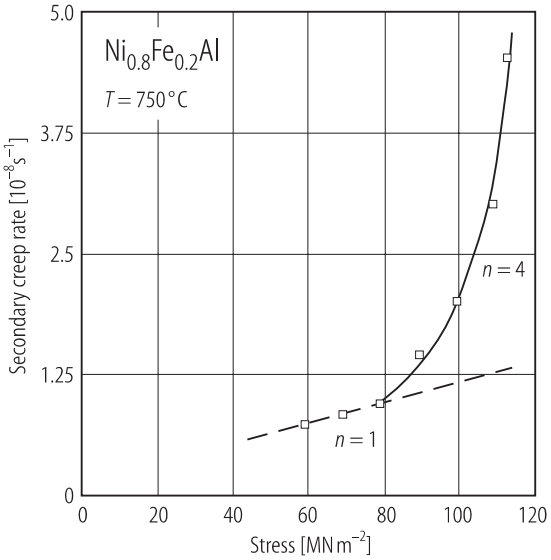

Fig. 14. Stress dependence of the secondary creep rate of $(Ni_{0.8}Fe_{0.2})Al$ at 750 °C [87J1]. *n*: power law dependence of creep rate on stress.

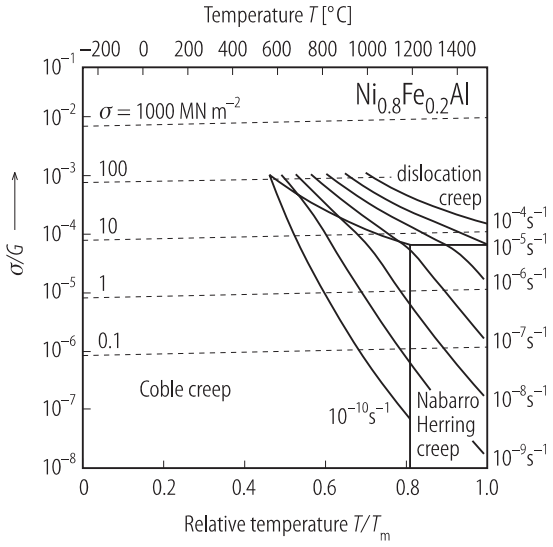

Fig. 15. Deformation map for $(Ni_{0.8}Fe_{0.2})Al$ with a diffusion length of 100 µm for diffusion creep (G = shear modulus, T_m = melting point, the dashed lines are contours of constant strain rate) [87J1].

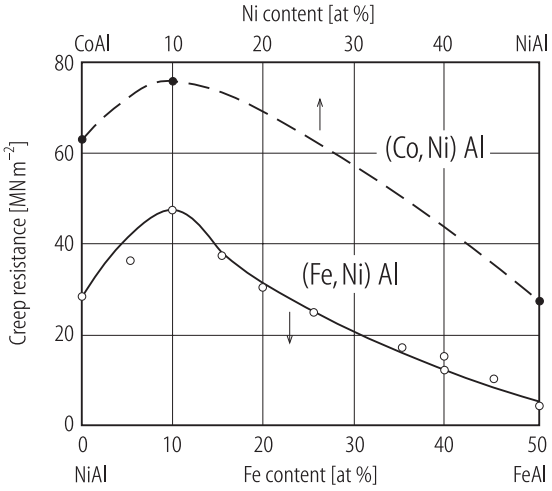

Fig. 16. Compositional dependence of the creep resistance (at $10^{-7}s^{-1}$) at 900 °C of (Co,Ni)Al and (Fe,Ni)Al [87J1].

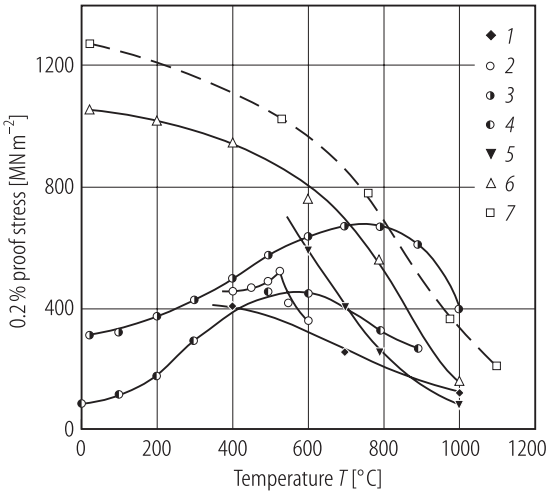

Fig. 17. Temperature dependence of the 0.2 % proof stress for $(Ni_{0.8}Fe_{0.2})Al$ (*1*), Fe_3Al (*2*), advanced Ni_3Al (*3*), Ni_3Al (*4*), Fe_3AlC with graphite (*5*), Ni_3AlC (*6*), and MA 6000 (*7*) [87J1].

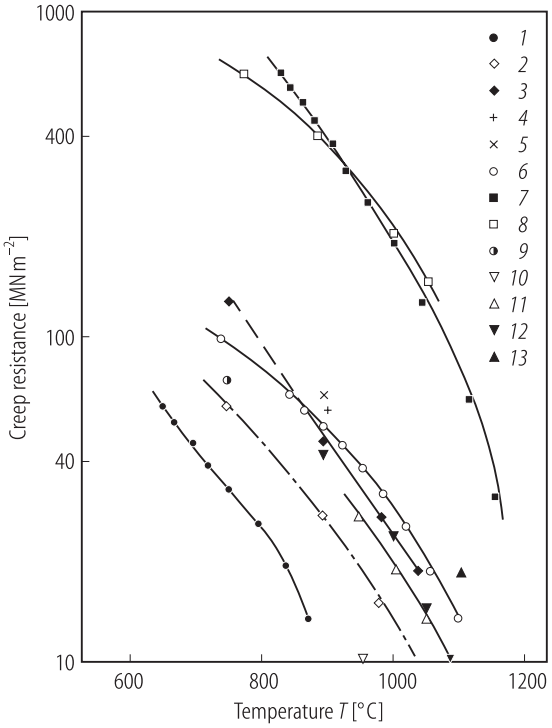

Fig. 18. Temperature dependence of the creep resistance (at $10^{-7}s^{-1}$) for single-crystalline NiAl (*1*), polycrystalline NiAl (*2*), $(Ni_{0.8},Fe_{0.2})Al$ (*3*), CoAl (*4*), $(Co_{0.8}Ni_{0.2})Al$ (*5*), Ni_2AlTi (*6*), Ni_2AlTi with precipitated NiAl (*7*), MAR-200 (*8*) advanced Ni_3Al (*9*), Fe_3AlC with precipitated αFe (*10*), Ni_3AlC (*11*), Fe_3AlC with precipitated graphite (*12*), and $NbAl_3$ (*13*) [87J1].

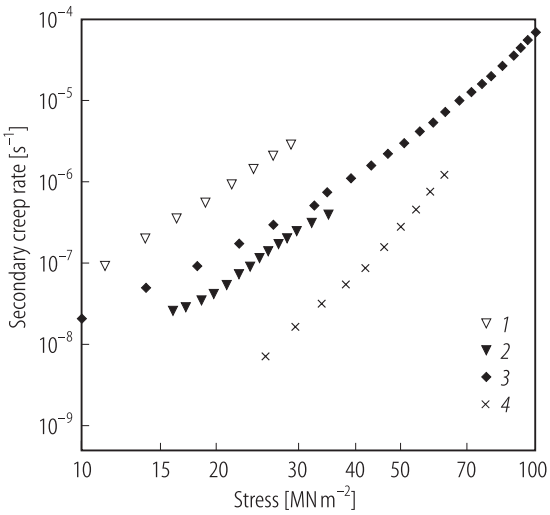

Fig. 19. Stress dependence of the secondary creep rate of Fe_3AlC with αFe precipitate at 950 °C (*1*), Fe_3AlC with graphite at 1000 °C (*2*), $(Ni_{0.8}Fe_{0.2})Al$ at 1027 °C (*3*), and $(Co_{0.8}Ni_{0.2})Al$ at 1027 °C (*4*) [87J1].

Ni–Hf–Al

The microstructure and mechanical properties of several Ni–Al–Hf samples have been studied in the compositional range (NiAl) (β) and Ni_2HfAl (Heusler phase). The volume fraction V_f of the Heusler phase varies from 15 % to 96 %. The yield strength increases with increasing V_f at all temperatures up to 1000 °C. All the alloys can be extensively deformed without fracture at 1000 °C. The hardness of the Heusler alloy is very high (8.3 GPa) at room temperature but slowly decreases up to 600 °C and then rapidly falls off. The brittleness and high hardness at low temperatures is related to lattice distortions.

Table 3. Phases present, lattice parameter *a* and volume fraction of Heusler phase, V_f, in HH-1, HH-2 and HH-4 [90T3].

Alloy	Phase present	*a* [Å]	V_f [%]
HH-1	B2	2.886	14.7
	$L2_1$	6.070	
HH-2	B2	2.885	47.9
	$L2_1$	6.069	
HH-4	$L2_1$	6.061	> 96
	unknown	[a])	

[a]) Cannot be determined.

Table 5. Estimation of lattice strain ε in the Heusler structure from atomic spacing Ni–Al, Ni–Hf and Ni–Ti pairs in B2 and Heusler structures [90T3].

Atomic pair	d^B_{AB} [Å]	d^B_{AC} [Å]	$d^H_{AB=AC}$ [Å]	ε [%]
Ni–Al	2.500		2.624	5.0
Ni–Hf		2.740	2.624	– 4.2
Ni–Al	2.500		2.530	1.2
Ni–Ti		2.611	2.530	– 3.1